Physics of Plasmas

Supersonic jet generation by underwater sub-microsecond electrical explosions of wire arrays

Cite as: Phys. Plasmas **29**, 032705 (2022); https://doi.org/10.1063/5.0083419
Submitted: 25 December 2021 • Accepted: 05 March 2022 • Published Online: 21 March 2022
Published open access through an agreement with Inter-University Computation Center

D. Maler, M. Kozlov, S. Efimov, et al.

Physics of Plasmas ARTICLE scitation.org/journal/php

Supersonic jet generation by underwater sub-microsecond electrical explosions of wire arrays

Cite as: Phys. Plasmas **29**, 032705 (2022); doi: 10.1063/5.0083419
Submitted: 25 December 2021 · Accepted: 5 March 2022 ·
Published Online: 21 March 2022

D. Maler,[1,a)] M. Kozlov,[2] S. Efimov,[1] and Ya. E. Krasik[1]

AFFILIATIONS

[1]Physics Department, Technion, Haifa 320003, Israel
[2]Center for Preparatory Studies, Nazarbayev University, Nur-Sultan 010000, Kazakhstan

[a)]Author to whom correspondence should be addressed: daniel.maler@campus.technion.ac.il

ABSTRACT

Experiments in which supersonic water jets are generated by underwater sub-μs timescale electrical explosions of cylindrical and conical wire arrays are presented. These are compared with previous experiments [Maler *et al.*, Phys. Plasmas **28**, 063509 (2021)] in which the generation of supersonic water jets was demonstrated using a μs timescale generator. Although in the present experiments less energy is deposited into the wire arrays, the water jets acquire higher velocities compared to when the deposited energy is higher but the timescale is slower. That is, with a higher energy density deposition rate, faster radial wire expansion is induced resulting in a stronger converging shockwave and a faster waterflow behind its front. In addition, two dimensional hydrodynamic numerical simulations show that the formation of the water jet is the result of extremely high pressure at the axis of the shockwave implosion and the cumulative edge effect realized at the array output.

I. INTRODUCTION

The field of high energy density physics, exploring exotic states of matter, has developed significantly during the last eighty years or so. Large facilities such as the Z-machine[2,3] and the National Ignition Facility (NIF)[4,5] realize extreme states of matter, contributing to the expanding knowledge on the behavior of matter in the extreme environments of planetary astrophysics[6] and inertial confinement fusion.[7] Using moderate power pulsed generators, with stored energy of several kJ, underwater electrical explosions of wire arrays have proved to be a compact and an accessible approach for studying matter at extreme conditions in a university laboratory. One application of this approach was demonstrated in our previous article[1] where the generation of supersonic jets with velocities up to 4 km/s and pressure up to 10^{10} Pa was realized by an electrically exploding μs-timescale wire array of cylindrical and conical geometry. These supersonic jets can be potentially utilized for studies in high energy density physics, research of hydrodynamic (HD) instabilities and possibly the exploration of the low energy d–d reaction cross section.

The experimental setup in the experiment described in the present article is similar to that in Ref. 1, apart from the sub-μs generator used,[8] characterized by a higher energy density deposition rate, replacing the μs timescale generator used earlier. Two-dimensional (2D) hydrodynamic (HD) FLASH[9] simulations coupled with the Sesame[10] Equations of State (EOS) for water were carried out, using as input data the experimentally determined power deposited into the wires. These simulations aim to approximate experimental conditions and explain the mechanism responsible for the supersonic water jets generation.

II. EXPERIMENTAL SETUP

The high-current pulse generator MAGEN[8] was used to power the underwater electrical explosion of cylindrical and conical copper wire arrays. The generator, of 1.92 μF capacity, was charged up to 75 kV (5.4 kJ stored energy). The wire array consisted of 40 wires, each wire having 114 μm diameter. The distance between the high voltage (HV) and ground electrodes was designed to be 40 mm for both cylindrical and conical configurations. These array parameters correspond to an almost critically damped discharge when most of the stored energy is deposited into the wires during a time comparable to a quarter period of an underdamped discharge. The diameter of the wire array was 10 mm for a cylindrical configuration. For a conical array, the upper high voltage (HV) electrode had a 10 mm diameter hole (the HV electrode in Fig. 1) and the bottom electrode had a 5 mm

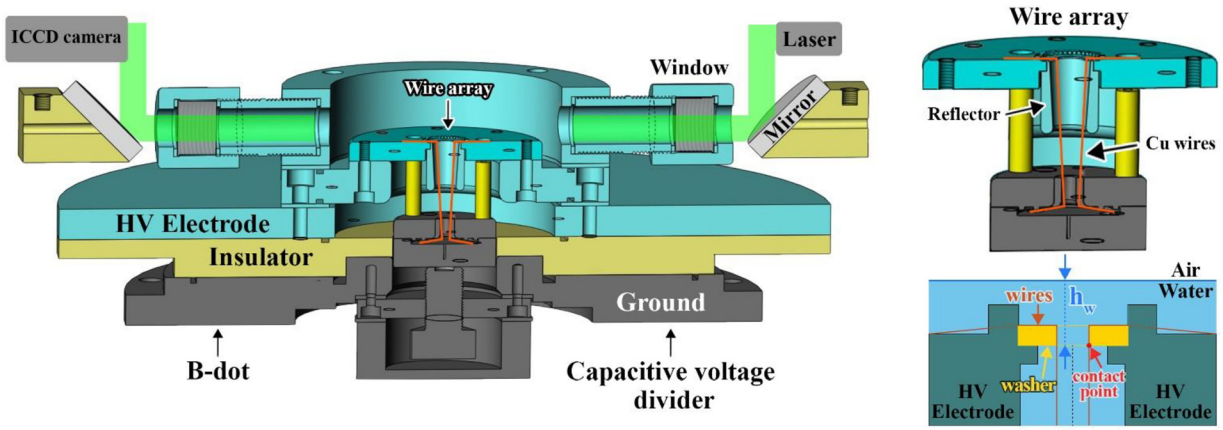

FIG. 1. Experimental chamber attached to the MAGEN generator (left), conical Cu wire array fitted with a conical stainless-steel reflector (right-top) and an enhanced view of the HV electrode (right-bottom).

diameter hole (Ground in Fig. 1), resulting in a half apex angle of 3.58°. For each array geometry, a stainless-steel cylindrical reflector was fitted, encompassing the wire array, reflecting the outward water-flow and part of the divergent shock toward the symmetry axis of the array.[1] The reflector, 25 mm long, 3 mm thick, and 14 mm diameter, was connected to the HV electrode (see Fig. 1) keeping a distance of 2 mm between the wires and the inner wall of the reflector. The 25 mm long conical reflector was designed to also maintain a distance of 2 mm between its inner wall and the wires. The distance of 15 mm between the reflector smoothed edge and the ground electrode prevents any possible breakdowns. The wire array was submerged in de-ionized water having a resistivity of ∼1 MΩ cm. The total resistance between the edge of the reflector to the grounded electrode was in the range of 1–5 kΩ. Thus, for a maximal voltage of 75 kV, the amplitude of the current losses to the water does not exceed several ten of Ampère which is negligible with respect to the discharge current amplitude (>350 kA).

A short circuit test was performed at 70 kV to estimate the inductance of the experimental setup and for calibrating the D-dot voltage probe using a commercial P6015A Tektronix divider. Current measurements were performed by integrating the signal obtained by a B-dot probe. The total inductance of the discharge circuit was found to be ∼42 nH, and the inductance of the wire array load $L_{load} \sim 25$ nH. The array resistive voltage φ_{res} was calculated by subtracting the induced voltage from the total voltage V as $\varphi_{res} = V - L_{load}(dI/dt)$. All calculated values of energy, derived from experimental power, were estimated to have an error of ∼3%.

The array, submerged into the de-ionized water, was placed inside the experimental chamber (see Fig. 1). The 15 mm thick HV electrode has a 20 mm diameter central hole where a 10 mm inner diameter and 0.8 mm thick washer was soldered. The distance from the bottom of the washer, where the wires contact is made, to the upper surface of the HV electrode was of 1.6 ± 0.1 mm. The water level, initially 0.4 ± 0.1 mm above the upper surface of the HV electrode, was measured using an XXRapidFrame ICCD multi-channel framing camera (Stanford Computer Optics Inc.). Thus, the water level, defined relative to the wire contact point with the HV electrode,[1] was measured to be $h_w = 2 \pm 0.1$ mm for all explosions. The HV electrode, water, and air were backlit by a CW single mode laser (532 nm), directed by a mirror as shown in Fig. 1, to produce shadow images of the water jet propagation in air, recorded using the fast framing camera. By producing a sequence of images, with a known time interval between frames, we calculate the jet velocity. Due to the smearing of the jet front, the error in the velocity measurement δv_{jet} was calculated to be ±120 m/s.

III. EXPERIMENTAL RESULTS

Typical waveforms of the current and resistive voltage for 75 kV charging voltage of MAGEN along with the power and energy deposited into the wire array are shown in Fig. 2. One can see that the current reaches ∼400 kA with a rise time of ∼400 ns and the discharge is

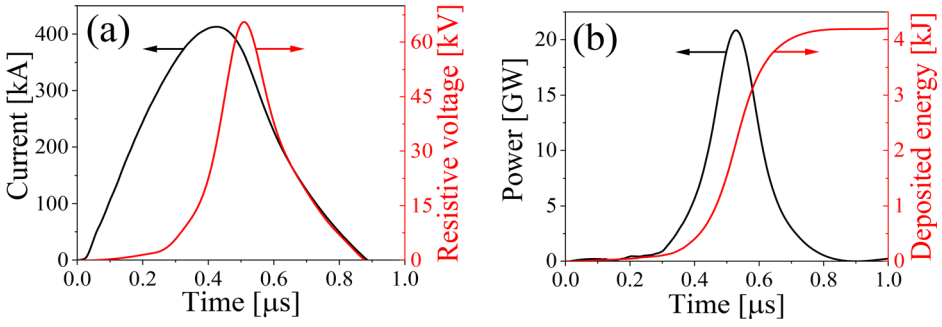

FIG. 2. Typical waveforms of the current and resistive voltage (a) and the deposited power and energy (b) for the MAGEN generator for a charging voltage of 75 kV.

TABLE I. Comparison of different timescale generator parameters.

	Stored energy (kJ)	Charging voltage (kV)	Deposited energy (kJ)	$\alpha = \frac{\text{deposited energy}}{\text{stored energy}}$	Energy density deposition (MJ/kg)	Energy density deposition rate [MJ/(kg s)] $\times 10^6$
μs generator	5.4	33	5.1	0.94	35	90
MAGEN generator	5.4	75	4.2	0.77	28.8	120

almost critically damped where half of the energy stored in MAGEN is deposited into the wires within ~150 ns. The energy deposited into the wires during the first ~900 ns is calculated relative to the beginning of the discharge current.

The discharge parameters for the previously used μs-timescale generator (in short, the μs generator) and the MAGEN generator for the same stored energy are compared in Table I. The energy density deposition rate in explosions driven by MAGEN is typically ~1.3 times higher than that driven by the μs generator. This value was calculated for each generator by evaluating the deposited energy density within the full pulse duration at half maximum of the deposited power. The smaller value of α in Table I. for MAGEN is related to the slightly underdamped discharge which is not optimal for most efficient energy deposition rate into the wires. One can see that although the deposited energy density for the μs generator is 21% higher than for MAGEN, for the same stored energy, the energy density deposition rate is 33% higher for sub-μs explosions.

For the two generators we explored two configurations for both cylindrical and conical arrays. For each array geometry, an explosion with and without the reflector (see Sec. II) was carried out. The results with MAGEN for all configurations are compared with our previous results[1] in Table II.

One can see that for both array geometries the jet velocity is slightly larger for MAGEN explosions than with the μs generator within the given error when no reflector is used, even though the deposited energy density is lower. With a reflector, the velocity increase becomes substantial for MAGEN explosions. This important result can be attributed to the higher MAGEN energy density deposition rate which in turn determines the wire expansion velocity and subsequently, a higher shock velocity.

In Figs. 3(a) and 3(b), we see the shadow images of water jets generated by the explosion of a cylindrical array without a reflector where a jet velocity of ~3400 m/s was realized. In Figs. 3(c) and 3(d), the water jet, formed by the explosion of a conical array fitted with a reflector, propagated with a velocity of ~3900 m/s. In images where the jet propagated several mm, a Mach cone is visible around the sides

TABLE II. Experimental jet velocities for different timescale generators ($\delta v_{jet} = \pm$ 120 m/s).

Configuration	Reflector	Jet velocity μs generator[1] (m/s)	Jet velocity MAGEN generator (m/s)
Cylindrical	No	3100	3400
Cylindrical	Yes	3100	3600
Conical	No	3200	3500
Conical	Yes	3400	3900

of the water jet. The Mach angles estimated from Fig. 3 were $\alpha_M \sim 5.6^\circ$ and $\alpha_M \sim 4.8^\circ$ for cylindrical without a reflector and conical with a reflector array explosions, respectively. The jet velocity $v = c_{air}/\sin\alpha_M$, where c_{air} is the sound speed in undisturbed air, estimated using the angle α_M of the Mach cone, yields 3380 and 3940 m/s for $\alpha_M \sim 5.6^\circ$ and $\alpha_M \sim 4.8^\circ$, respectively. These values coincided with the time of flight measurements performed using the shadow images.

IV. NUMERICAL MODELING OF THE JET FORMATION

The formation of a jet by a converging shock generated by underwater electrical explosion of wire arrays involves interaction of radially expanding wires, water, and air at the dynamically evolving interfaces between them. FLASH, a parallel, adaptive mesh, multi-physics code developed at the University of Chicago,[9,11] that we used to implement our numerical model, is limited. Because of this, we consider a reduced model where energy is deposited only into an either cylindrical or conical layer of water. Also, because of the absence of exploding wires, we performed these simulations without accounting the reflector which was used in part of experiments. This approach significantly simplifies the problem yet it includes all the essential processes of jet formation: the generation and implosion of the shock wave. To simulate the formation of the jet by a converging shock wave in water we solve Euler's equations, namely, the mass, momentum, and energy conservation equations:

$$\frac{\partial \rho}{\partial t} + \nabla \cdot (\rho \boldsymbol{v}) = 0, \tag{1}$$

$$\frac{\partial \rho \boldsymbol{v}}{\partial t} + \nabla \cdot (\rho \boldsymbol{v}\boldsymbol{v}) + \nabla P = 0, \tag{2}$$

$$\frac{\partial \rho E}{\partial t} + \nabla \cdot [(\rho E + P)\boldsymbol{v}] = 0. \tag{3}$$

Here, ρ, P, and $\boldsymbol{v}$ are the density, pressure, and velocity of water, respectively, and E is the total specific energy (energy per unit mass) which is the sum of the internal and kinetic specific energies $E = \varepsilon + \boldsymbol{v}\boldsymbol{v}/2$. These equations are coupled to EOS[10] for water

$$\varepsilon = \varepsilon(\rho, T), \tag{4a}$$

$$P = P(\rho, T), \tag{4b}$$

where T is the water temperature. In regions where the total energy is dominated by kinetic energy, computing the internal energy as $\varepsilon = E - \boldsymbol{v}\boldsymbol{v}/2$ can lead to significant truncation error which in turn results in inaccurate values of pressure and temperature. To overcome this problem, an additional equation for the internal energy

$$\frac{\partial (\rho \varepsilon)}{\partial t} + \nabla \cdot [(\rho \varepsilon + P)\boldsymbol{v}] - \boldsymbol{v} \cdot \nabla P = 0, \tag{5}$$

was evaluated, if the internal energy was below 10^{-4} of the kinetic energy. Euler's equations were solved in cylindrical coordinates with

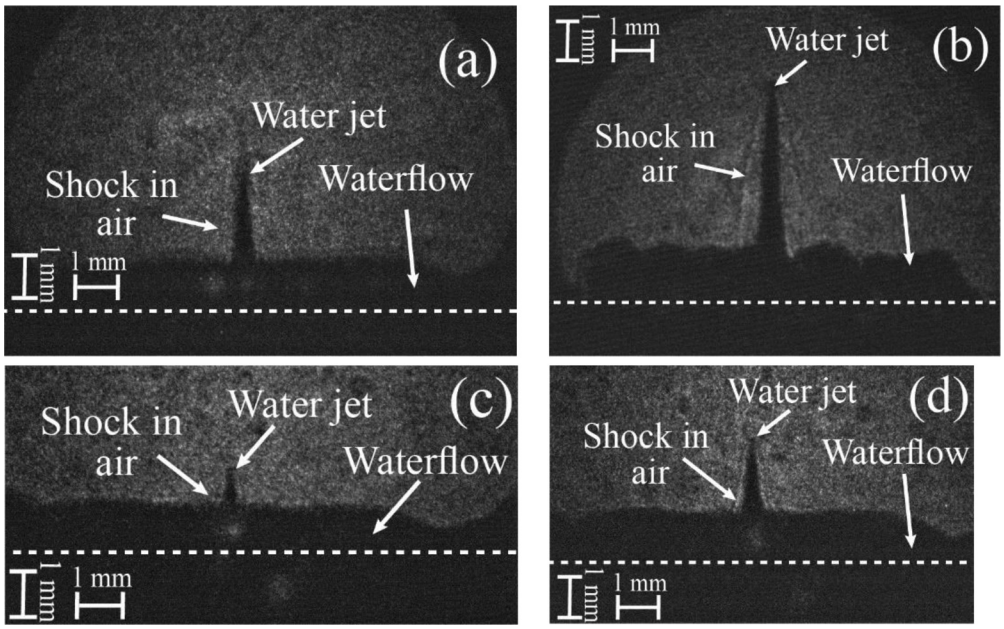

FIG. 3. Shadow images of a water jet, generated by the explosion of cylindrical array without a reflector at t = 4.4 μs (a) and at 5.5 μs (b) and the explosion of a conical array with a reflector at t = 3.2 μs (c) and at 3.7 μs (d), respectively. The time is measured with respect to the beginning of the current discharge. The dashed line marks the initial water level.

azimuthal symmetry, which implies dependence of all HD parameters on radius r and height z. Cylindrical and conical geometries without a reflector were considered as shown in Figs. 4(a) and 4(b), where the yellow areas represent regions of energy deposition into the water layer and the dark red areas are electrodes. The red and green lines indicate

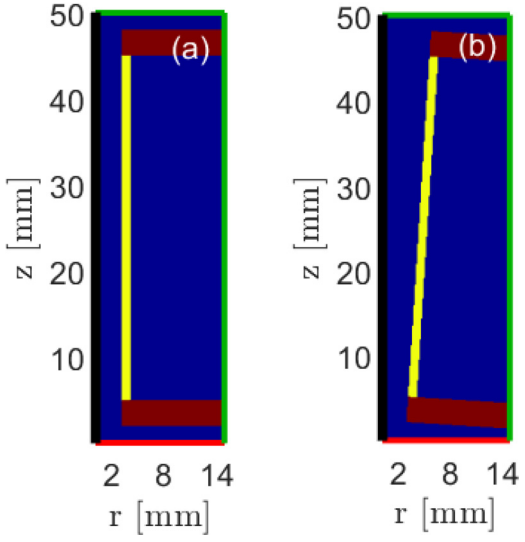

FIG. 4. Simulation domains with cylindrical (a) and conical (b) geometries without a reflector. Yellow areas represent regions of energy deposition and dark red areas are the electrodes holding the wire arrays. Red and green lines indicate reflecting and outflow BC, respectively.

reflecting or outflow boundary conditions (BC), respectively. The outflow BC were assigned by imposing zero gradient HD parameters across the border. The $r = 0$ line is an axis of symmetry. The internal radius of energy deposition into the water layer was 4.5 mm, which is smaller than the radius of the experimental wire array (5 mm). This difference is a rough approximation of the expansion of the wires during the heating, melting and vaporization phases, i.e., prior to the wire transforming into a partially ionized, high resistivity vapor-plasma state,[12] characterized by the main energy deposition phase.

We simulated experiments with both μs and sub-μs electrical discharges into the wire arrays. Figure 5 represents the experimental power deposition rates for the μs (red solid curve) and sub-μs (blue solid curve) timescale experiments (see Sec. III) and the Lorentzian approximation (dashed lines) of the corresponding experimental power used in the simulations. The total deposited energy was close to 5 kJ for both cases. The calculated deposited power was multiplied by an efficiency coefficient (0.7) to reproduce the experimentally obtained "time of flight" of the shock toward the axis.

The numerical solution of the HD equations (1)–(3) was obtained by a directionally unsplit Monotone Upstream-centered Scheme for Conservation Laws (MUSCL)[13,14] with a Haten, Lax, and van Leer (HLL) Riemann solver[15] used for computing Godunov's flux. The MUSCL method provides second-order solution accuracy for smooth flows and first-order accuracy for shock flows in both space and time. This numerical scheme is implemented in the FLASH computational software that we used for our simulations.[9,16] One of the main advantages of the FLASH simulation software is adaptive mesh refinement. In our simulations, the minimal resolution, applied at the shock front, was ~20 μm, whereas up to ~200 μm resolution was used for the regions with small gradients. Pressure was calculated from

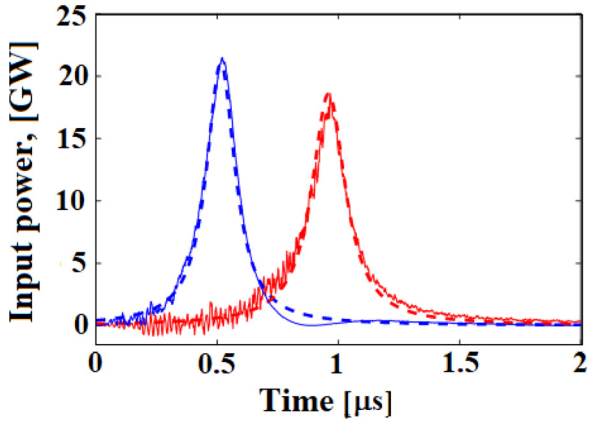

FIG. 5. Energy deposition rates for the μs (red solid curve) and sub-μs (blue solid curve) experiments. The dashed curves of corresponding color represent Lorentzian approximations of the corresponding experimental deposition rates that were used in the simulations.

tabulated EOS [Eqs. 4(a) and 4(b)] for water[10] using a two-dimensional spline-interpolation algorithm. In addition, the speed of sound c_s required by the HLL Riemann solver was computed as

$$c_s = \sqrt{\frac{P}{\rho^2}\frac{\partial P/\partial \rho}{\partial \varepsilon/\partial T} + \frac{\partial P}{\partial \rho} - \frac{\partial P}{\partial T}\frac{\partial \varepsilon/\partial \rho}{\partial \varepsilon/\partial T}}, \tag{6}$$

with temperature $\partial P/\partial T$, $\partial \varepsilon/\partial T$ and density $\partial P/\partial \rho$, $\partial \varepsilon/\partial \rho$ derivatives obtained by differentiating the corresponding spline polynomials.

Results of simulations of the jet formation for the case when the energy was deposited into a cylindrical water layer on the sub-μs timescale are presented in Figs. 6 and 7. Similar results were obtained for a conical water layer. The pressure distribution at $t = 2.27$ μs, shown in Fig. 6(a) with enlarged regions seen in Figs. 6(b) and 6(c) illustrate the beginning of the jet formation as an expansion of water from the region of extremely high ($\sim 3 \times 10^{10}$ Pa) pressure. This pressure is the result of the implosion of the shock in the vicinity of the axis. The jet propagates into the funnel-shaped region of water formed by the front of the converging shock at the output of the array. The distribution of the vertical velocity in the $[z, r]$ plane at $t = 2.27$ μs is depicted in Fig. 6(d) [Figs. 6(e) and 6(f) show enlarged areas of Fig. 6(d)] at the time when the highest jet velocity is achieved at the tip of the compressed region where the pressure gradient is highest.

The dynamics of the jet development is displayed in Fig. 7 for different times relative to the beginning of the energy deposition into the water layer. The first row depicts distribution of the pressure [Fig. 7(a)], density [Fig. 7(b)], and velocity [Fig. 7(c)] along the axis of the wire array. The second row depicts radial distribution of the maximal values of the pressure [Fig. 7(d)], density [Fig. 7(e)], and velocity [Fig. 7(f)] over the cross section at which the maximum of the respective parameter's axial distribution occurs. On axis, one can see that the pressure and density decrease as the jet propagates inside the undisturbed water [Figs. 7(a) and 7(b)]. In spite of the decrease in pressure and density, the jet velocity increases up to $z \sim 45$ mm [Fig. 7(c)]. So, one can conjecture that the maximum in the jet velocity is related to two processes, namely, the jet acceleration by the pressure gradient and the cumulative effect of the converging water flow formed at the output of the cylindrically expanding water layer followed by deceleration of the jet during its propagation through stationary water.

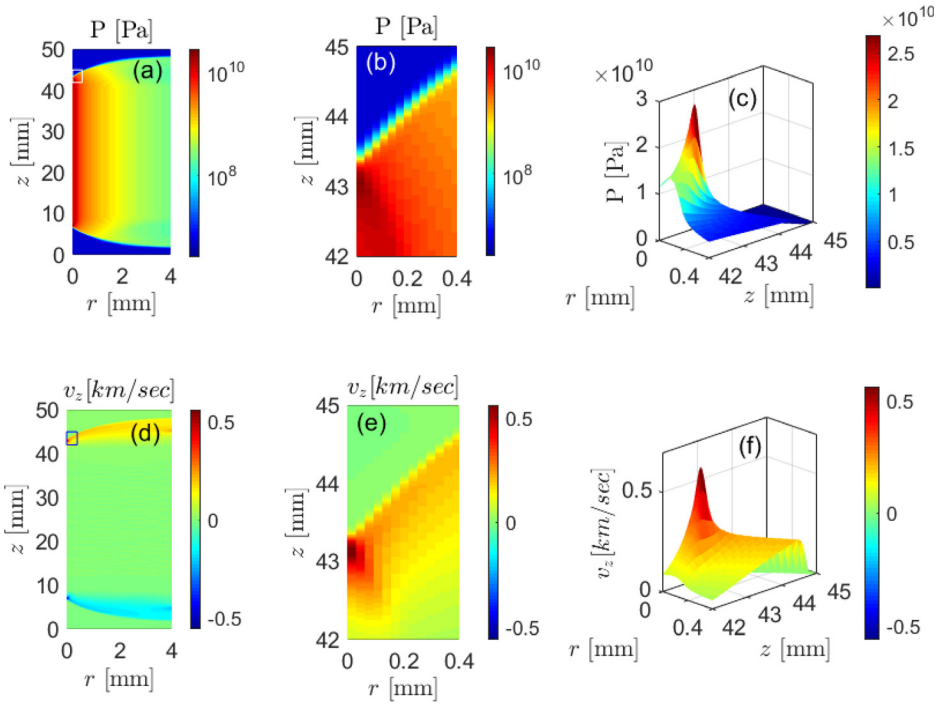

FIG. 6. Distribution of pressure (a) and (c) and vertical velocity (d) and (f) at $t = 2.27$ μs (beginning of the jet formation). The enlarged areas of pressure (b) and (c) and the corresponding velocity (e) and (f) are denoted by rectangles in (a) and (d).

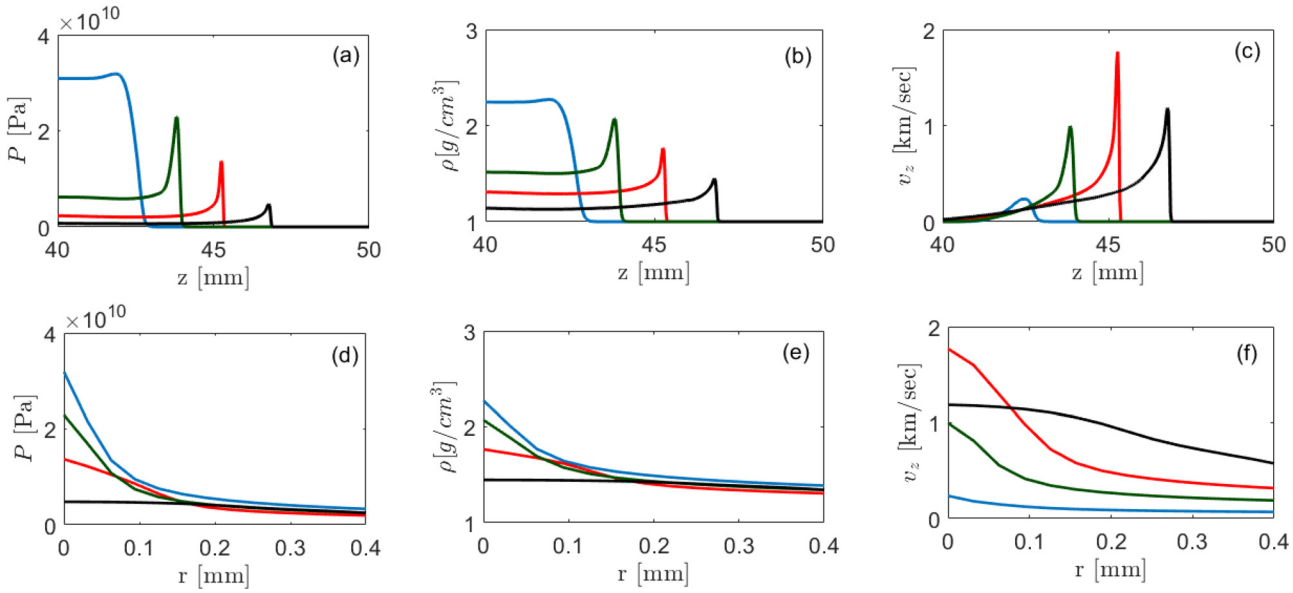

FIG. 7. Dynamics of the jet development. Axial distributions of pressure (a), density (b), and velocity (c) and radial distribution of pressure (d), density (e), and velocity (f) at the maximum values of the corresponding parameter. Different times are represented by curves of different color: $t = 2.27$ μs (blue), $t = 2.37$ μs (green), $t = 2.48$ μs (red), and $t = 2.78$ μs (black). Here the scale along the z-axis corresponds to Figs. 6(a), 6(b), 6(d), and 6(e) scale.

In Table III, we list the maxima of the simulated jet velocities for cylindrical and conical (half aperture angle of 3.58°) geometries of the water layer for different energy deposition rates and total deposited energies. Quantitatively the obtained numerical data do not coincide with experimental results, and this issue will be addressed below. One can see that the increase in the energy density deposition rate leads to insignificant increase in the jet velocity. However, an increase in the deposited energy by a factor of 10 results in the increase in the maximum jet velocity by a factor of 3. Thus, the maximum jet velocity scales approximately as the square root of the deposited energy. Numerical results suggest that the maximum jet velocity is a complicated function resulting from the interplay between the energy, the energy deposition rate, and the aperture angle of the wire array. Increasing the energy deposition rate by 10% for the same total deposited energy results in an increase in the maximum jet velocity by only 1%. On the other hand, for μs-timescale energy deposition, the total energy deposited into the water layer was ∼3% higher than that obtained in the sub-μs simulations but the energy density deposition rate was ∼11% slower. This resulted in almost identical values of the maximum jet velocity for both cases.

Dependence on the aperture angle for the conical geometry is probably even more complex. For μs- and sub-μs timescale energy deposition, the maximum jet velocity for the conical geometry is slightly (∼6%) higher than in cylindrical geometry. However, when the deposited energy increases by a factor of 10, the maximum jet velocity obtained for conical and cylindrical geometries become almost identical. The study of the dependence of jet velocity on the amount of deposited energy, energy deposition rate, and angle of aperture can be an interesting subject for future research.

As mentioned above, no quantitative agreement between numerical and experimental results was obtained. The reason for this is probably that in contrast to the experimental setup, the simulation accounts only for water, that is, there is no air interface for the high speed waterflow to reload through. Moreover, the wire material was also replaced by water which could affect the efficiency of the energy deposition into the water flow. However, qualitative agreement was obtained, with the result that for long distance propagation of the water jet through water, we obtain large losses in kinetic energy, the result of friction with stationary water of given viscosity.

TABLE III. Simulated jet velocities for different values of the deposited energy and energy density deposition rates.

	μs-timescale energy deposition. Total deposited energy 4.94 kJ	Sub-μs timescale energy deposition. Total deposited energy 4.79 kJ	Energy deposition rate 10% faster than sub-μs timescale. Total deposited energy 4.79 kJ	Ten times higher deposited energy than in sub-μs timescale. Total deposited energy 49.4 kJ
Cylindrical geometry	1.77×10^3 m/s	1.77×10^3 m/s	1.79×10^3 m/s	5.21×10^3 m/s
Conical geometry	1.91×10^3 m/s	1.88×10^3 m/s	1.91×10^3 m/s	5.19×10^3 m/s

V. SUMMARY

Experimental and numerical results of the supersonic water jet generated by underwater electrical explosions of cylindrical and conical wire arrays were presented for the sub-μs MAGEN generator. In these experiments, with less energy density deposited into the wire array an increase in jet velocity was obtained compared to previous experiments with a μs timescale generator. This result is attributed to the increased (up to 33%) energy density deposition rate realized by the sub-μs timescale generator. As previously suggested,[1] the numerical study of the jet formation strongly suggests that the formation of a supersonic water jet by the implosion of axially symmetric wire arrays is governed by two processes: (a) the cumulative edge effect of converging shock at the array boundaries and (b) the extreme water parameters at the axis of implosion. These water jets can be the subject of additional experimental work such as the study of jet interaction with a target, two colliding heavy water jets and their interaction complemented by additional hydrodynamic simulations including the presence of the wire material, the water–air interface, and hydrodynamic instabilities.

ACKNOWLEDGMENTS

We are grateful to Dr. A. Rososhek, Dr. S. Bland, and Dr. J. G. Leopold for fruitful discussions and S. Gleizer, E. Flyat, R. Samana, and L. Merzlikin for generous technical assistance. The software FLASH used in this work was developed largely by the Flash Center for the Computational Science currently hosted by the Department of Physics and Astronomy of the University of Rochester. This research was supported by the Israeli Science Foundation Grant No. 492/18.

AUTHOR DECLARATIONS

Conflict of Interest

The authors have no conflicts to disclose.

Author Contributions

D.M. and M.K. contributed equally to this work.

DATA AVAILABILITY

The data that support the findings of this study are available from the corresponding author and the FLASH parameter files are available from Dr. Maksim Kozlov upon reasonable request.

REFERENCES

[1]D. Maler, S. Efimov, A. Rososhek, S. N. Bland, and Y. E. Krasik, Phys. Plasmas **28**, 063509 (2021).
[2]D. B. Sinars, M. A. Sweeney, C. S. Alexander, D. J. Ampleford, T. Ao, J. P. Apruzese, C. Aragon, D. J. Armstrong, K. N. Austin, T. J. Awe *et al.*, Phys. Plasmas **27**, 070501 (2020).
[3]P. A. Gourdain, IEEE Trans. Plasma Sci. **43**, 2547 (2015).
[4]E. I. Moses, J. D. Lindl, M. L. Spaeth, R. W. Patterson, R. H. Sawicki, L. J. Atherton, P. A. Baisden, L. J. Lagin, D. W. Larson, B. J. MacGowan *et al.*, Fusion Sci. Technol. **69**, 1–24 (2016).
[5]A. Pribram-Jones, S. Pittalis, E. K. U. Gross, and K. Burke, *Frontiers and Challenges in Warm Dense Matter* (Springer, Cham, 2014).
[6]B. A. Remington, R. M. Cavallo, M. J. Edwards, D. D. M. Ho, B. F. Lasinski, K. T. Lorenz, H. E. Lorenzana, J. M. McNaney, S. M. Pollaine, and R. F. Smith, Astrophys. Space Sci. **298**, 235 (2005).
[7]V. A. Smalyuk, C. R. Weber, O. L. Landen, S. Ali, B. Bachmann, P. M. Celliers, E. Dewald, A. Fernandez, B. A. Hammel, G. Hall *et al.*, Plasma Phys. Controlled Fusion **62**, 014007 (2020).
[8]B. M. Kovalchuk, A. V. Kharlov, V. B. Zorin, and A. A. Zherlitsyn, Rev. Sci. Instrum. **80**, 083504 (2009).
[9]B. Fryxell, K. Olson, P. Ricker, F. X. Timmes, M. Zingale, D. Q. Lamb, P. MacNeice, R. Rosner, J. W. Truran, and H. Tufo, Astrophys. J. Suppl. Ser. **131**, 273 (2000).
[10]S. Lyon and J. Johnson, "The Los Alamos National Laboratory equation-of-state database," Report No. LA-UR-92-3407 (1992).
[11]A. Dubey, K. Antypas, M. K. Ganapathy, L. B. Reid, K. Riley, D. Sheeler, A. Siegel, and K. Weide, Parallel Comput. **35**, 512 (2009).
[12]A. Virozub, V. T. Gurovich, D. Yanuka, O. Antonov, and Y. E. Krasik, Phys. Plasmas **23**, 092708 (2016).
[13]V. L. Bram, J. Comput. Phys. **32**, 101 (1979).
[14]P. Colella, SIAM J. Sci. Stat. Comput. **6**, 104 (1985).
[15]A. Harten, P. D. Lax, and B. van Leer, SIAM Rev. **25**, 35 (1983).
[16]P. Tzeferacos, M. Fatenejad, N. Flocke, C. Graziani, G. Gregori, D. Q. Lamb, D. Lee, J. Meinecke, A. Scopatz, and K. Weide, High Energy Density Phys. **17**, 24 (2015).